ISSN: 2472-3703 DOI: 10.6911/WSRJ.202604_12(4).0002

Mechanical Resonance Suppression of Servo System Based on Resonant Frequency Online Identification

Lixiang Sun[1], Xiuwen Shan[1], Yi Zhang[2] and Hanpei Wei[2, *]

[1]Joint Technology Transfer Center of Yancheng Polytechnic College, Yancheng Polytechnic College, Yancheng 224005, China

[2]School of Automation, Jiangsu University of Science and Technology, Zhenjiang 212003, China

[*] Corresponding author

Abstract

This paper analyzes the mechanical resonance of permanent magnet AC servo systems and identifies the main factors that affect resonance. Further use fast Fourier transform for frequency online identification of the resonant system, and finally use a notch filter to filter the resonant frequency of the system. The impact of the notch filter on the system was analyzed and the parameters of the filter were determined, ultimately achieving the digitization of the notch filter. By analyzing the mechanical resonance system and identifying the resonance frequency online, the mechanical resonance of the permanent magnet AC servo system itself has been effectively suppressed. The experimental results have verified the effectiveness of the vibration suppression control algorithm.

Keywords

Mechanical resonance; Fast Fourier transform; Online identification; Notch filter.

1. INTRODUCTION

In view of the high-performance quality requirements of permanent magnet synchronous motor servo systems, problems existing in permanent magnet AC servo systems remain to be solved: the issue of mechanical resonance in servo systems caused by non-rigid load-connected equipment. In many applications, the motor and load of a servo system are not directly connected, but are usually linked via flexible transmission devices such as ball screws, pulleys, and gearboxes. These flexible components exhibit elastic characteristics. A typical example is found in industrial robots, where the drive motor and load of each joint are connected through a harmonic reducer to enhance the joint loading capacity. Since harmonic reducers feature flexible-load characteristics, a dual-inertia elastic system is formed among the motor, harmonic reducer, and load. During torque transmission, the motor shaft, load connection device, and load undergo different degrees of deformation, which easily triggers mechanical resonance. This resonance degrades the positioning accuracy of the servo system, and in severe cases, impairs system stability and causes physical damage to the mechanical components of the servo system.

In the early stages, the methods used to avoid mechanical resonance in permanent magnet servo systems mainly relied on reducing the slope of the reference command. Although this method can suppress vibration to a certain extent, it limits the bandwidth response of the servo system. At present, the suppression schemes for vibration problems in permanent magnet servo systems are generally divided into two categories: one is the active suppression scheme[1], and the other is the passive suppression scheme[2]. Active suppression schemes achieve vibration suppression by modifying the structure or adjusting the parameters of the three-loop system of

ISSN: 2472-3703 DOI: 10.6911/WSRJ.202604_12(4).0002

the controller, namely the position loop, velocity loop, and current loop. Examples include two-degree-of-freedom PI control[3, 4], state feedback control[5, 6], and some other advanced algorithms[7, 8]. Passive suppression methods filter the input reference of the three-loop system by designing appropriate filters. The vibration frequency of the system is first identified, and then a corresponding filter is configured based on this frequency to eliminate the vibration component from the input of the three-loop system, so as to achieve the purpose of vibration suppression[9, 10]. This method is widely used in the field of servo engineering. Among these filters, the notch filter[11] is the most widely used for suppressing input vibration signals.

In this paper, the mechanical resonance of permanent magnet AC servo systems is analyzed, and the main factors affecting resonance are obtained. Furthermore, the fast Fourier transform is adopted for online frequency identification of the resonant system. Finally, a notch filter is applied to filter out the resonant frequency of the system. The influence of the notch filter on the system is analyzed, and the parameters of the filter are determined, thus realizing the digitalization of the notch filter. Through the analysis of the mechanical resonance system and online identification of the resonant frequency, the inherent mechanical resonance of the permanent magnet AC servo system is effectively suppressed, and the performance of the system is improved.

2. MECHANICAL RESONANCE ANALYSIS OF PERMANENT MAGNET AC SERVO SYSTEMS

The model and block diagram of the two-inertia mechanical resonance system are shown in Figure 1 and Figure 2, respectively.

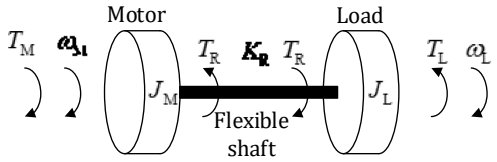

Figure 1. Two inertia resonance system model

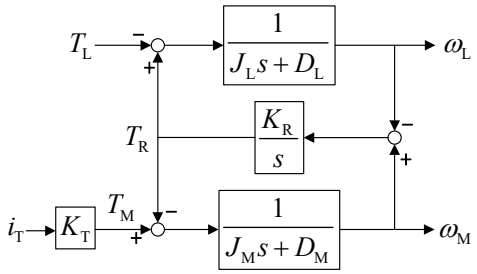

Figure 2. Principle block diagram of two inertia resonance system

The state equation and output equation of the system are as follows

$$\begin{bmatrix} \dot{\omega}_M & \dot{T}_R & \dot{\omega}_L \end{bmatrix}^T = A_p \begin{bmatrix} \omega_M & T_R & \omega_L \end{bmatrix}^T + B_p i_T + B_d i_L \tag{1}$$

$$\omega_M = C_p \begin{bmatrix} \omega_M & T_R & \omega_L \end{bmatrix}^T \tag{2}$$

ISSN: 2472-3703 DOI: 10.6911/WSRJ.202604_12(4).0002

where, $A_{\mathrm{p}}=\begin{bmatrix} -D_{\mathrm{M}}/J_{\mathrm{M}} & -1/J_{\mathrm{M}} & 0 \\ K_{\mathrm{R}} & 0 & -K_{\mathrm{R}} \\ 0 & -/J_{\mathrm{L}} & -D_{\mathrm{L}}/J_{\mathrm{L}} \end{bmatrix}$ 、 $B_{\mathrm{p}}=\begin{bmatrix} K_{\mathrm{T}}/J_{\mathrm{M}} & 0 & 0 \end{bmatrix}^{T}$ 、 $B_{\mathrm{d}}=\begin{bmatrix} 0 & 0 & -1/J_{\mathrm{M}} \end{bmatrix}^{T}$ 、 $C_{\mathrm{p}}=\begin{bmatrix} 1 & 0 & 0 \end{bmatrix}^{T}$.

Where J_{M} and J_{L} are the moments of inertia of the motor and the load, respectively; D_{M} and D_{L} are the rotational viscous friction coefficients of the motor and the load, respectively; ω_{M} and ω_{L} are the rotational angular velocities of the motor and the load, respectively; K_{R} is the torsional stiffness coefficient of the shaft; T_{R} is the shaft torque; i_{T} is the torque current of the motor; T_{L} is the load torque.

The simplified transfer function of the above system can be written as

$$P(s)=\frac{\omega_M}{i_T}\cong\frac{\left(K_T/J_M\right)\left(s^2+K_R/J_L\right)}{s\left(s^2+K_R/J_M+K_R/J_L\right)}=\frac{K_T/J_M}{s}\frac{s^2+\omega_a^2}{s^2+\omega_r^2} \tag{3}$$

where ω_{r} denotes a pair of complex conjugate poles of the system, corresponding to the resonant angular frequency; ω_{a} denotes a pair of complex conjugate zeros, corresponding to the anti-resonant angular frequency of the system.

$$\omega_{\mathrm{r}}=\sqrt{K_{\mathrm{R}}\left(\frac{1}{J_{\mathrm{M}}}+\frac{1}{J_{\mathrm{L}}}\right)} \tag{4}$$

$$\omega_{\mathrm{a}}=\sqrt{\frac{K_{\mathrm{R}}}{J_{\mathrm{L}}}} \tag{5}$$

At this point, the magnitude and phase characteristics of the mechanical resonance system are shown in Figure 3.

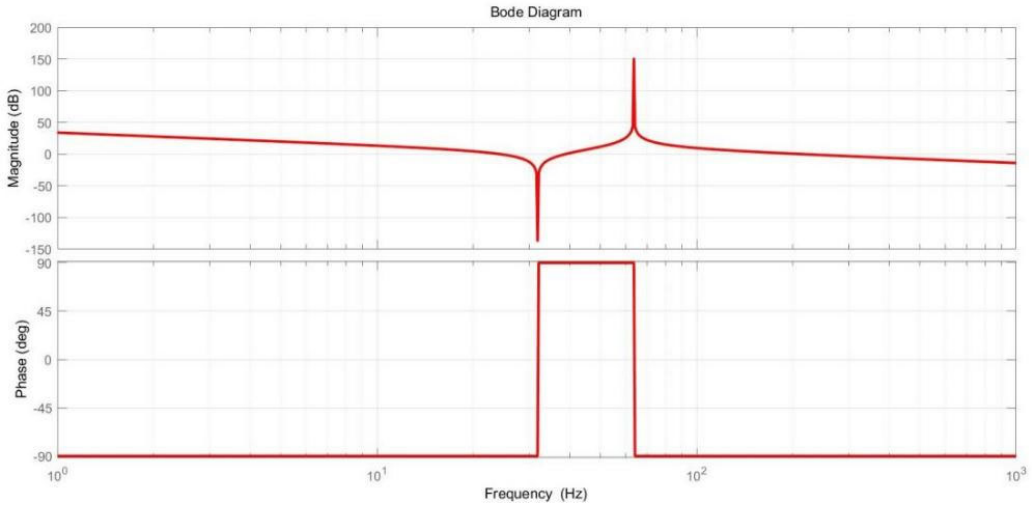

Figure 3. System Bode diagram

ISSN: 2472-3703 DOI: 10.6911/WSRJ.202604_12(4).0002

The main objective of mechanical resonance suppression in permanent magnet AC servo systems is to enable the load-side speed to track the reference speed without oscillations. As can be seen from Equation (4), the resonant frequency of the system is mainly affected by the inertia ratio J_L/J_M and the torsional stiffness coefficient K_{R} of the system. The influences of these two parameters on the resonant frequency of the system are analyzed separately in the following sections.

(1) Effect of Inertia Ratio on System Resonance

First, the inertia ratio of the system is defined as R.

$$R=\frac{J_{\mathrm{M}}}{J_{\mathrm{L}}} \tag{6}$$

The Bode plots of the system under different inertia ratios R are shown in Figure 4.

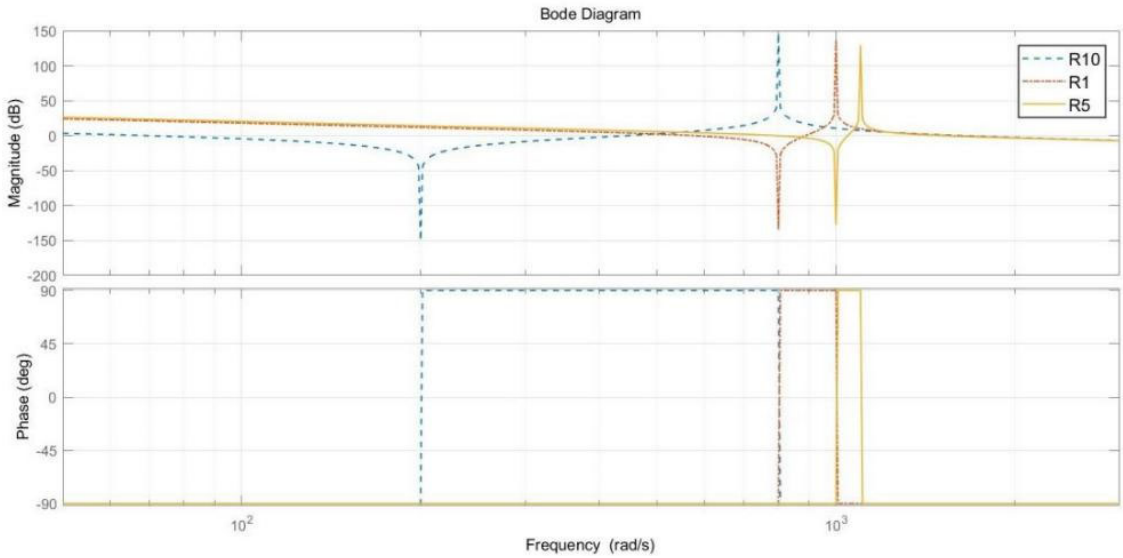

Figure 4. Bode diagram of system with different inertia ratio

The figure above shows the magnitude and phase characteristics of the system when the inertia ratio R is 0.5, 1, and 10, respectively. It can be seen from the figure that changing the inertia ratio will alter both the resonant frequency and the anti-resonant frequency of the system, thereby affecting the system performance. As the inertia ratio increases gradually, the difference between the anti-resonant frequency and the resonant frequency also increases, meaning that the anti-resonance performance of the system gradually deteriorates. It can be concluded that without any suppression measures, the larger the inertia ratio of the dual-inertia mechanical resonance system, the narrower the system bandwidth and the worse the dynamic performance.

Although the inertia ratio affects the system performance, its order of magnitude is relatively small. In addition, once a dual-inertia system is established, the inertia of the motor and the load generally remain unchanged. Therefore, the overall influence of the inertia ratio on the system performance is not significant, and the system is mainly affected by the torsional stiffness coefficient K_{R}.

(2) Effect of Torsional Stiffness Coefficient on System Resonance

ISSN: 2472-3703 DOI: 10.6911/WSRJ.202604_12(4).0002

The Bode plots of the system under different values of the torsional stiffness coefficient A are shown in Figure 5.

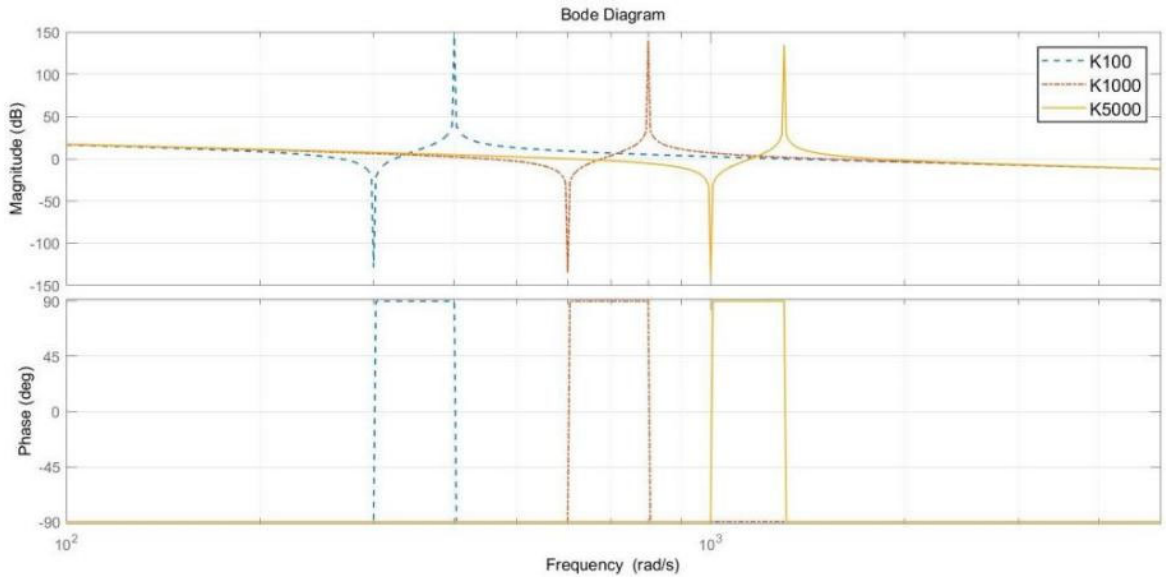

Figure 5. Bode diagram of systems with different rotational elastic coefficients

The figure above shows the magnitude and phase characteristics of the system when the torsional stiffness coefficient of the system is 100 $N \cdot m/rad$, 1000 $N \cdot m/rad$, and 5000 $N \cdot m/rad$, respectively. It can be seen from the figure that the larger the torsional stiffness coefficient, the higher the resonant frequency of the system. When the torsional stiffness coefficient is small, the resonant frequency may drop into the closed-loop bandwidth of the system, thereby causing mechanical resonance. However, the torsional stiffness coefficient cannot be changed once the system is built. Therefore, the influence of this coefficient on the system should be taken into account during system design, and a larger parameter value should be selected to improve system performance.

3. ONLINE IDENTIFICATION OF RESONANT FREQUENCY

As can be seen from the analysis in the previous subsection, mechanical vibration in the dual-inertia elastic system is mainly caused by a pair of complex conjugate poles introduced by the flexibility in the system. To eliminate this effect, the simplest method is to add a notch filter to the speed controller of the system, and place the zeros of the notch filter near the poles of the system to cancel the influence of these complex conjugate poles. During operation, the system is inevitably subjected to external disturbances, and its own parameters will also change with increasing operating time. Both factors will cause the resonant point of the system to shift. Once the resonant point shifts, the filtering effect of the pre-configured notch filter will be greatly reduced. Therefore, online identification of the system resonant frequency is particularly important. The block diagram of the dual-inertia mechanical resonance suppression system is shown in Figure 6.

ISSN: 2472-3703 DOI: 10.6911/WSRJ.202604_12(4).0002

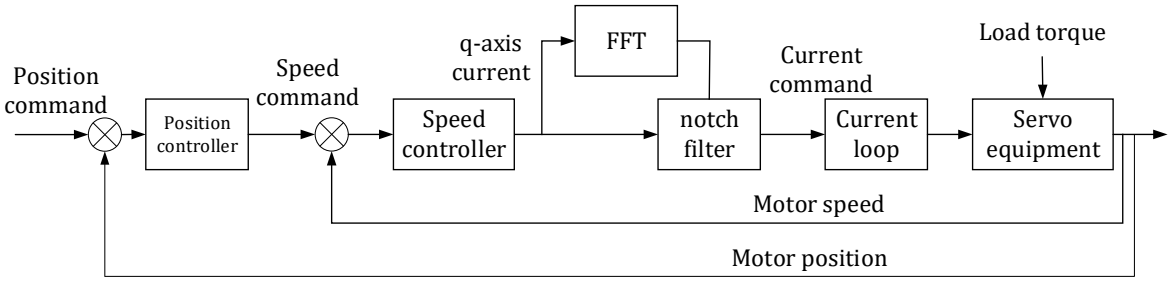

Figure 6. Principle block diagram of double inertia mechanical resonance suppression system

The block diagram of the resonant frequency detection part is shown in Figure 7.

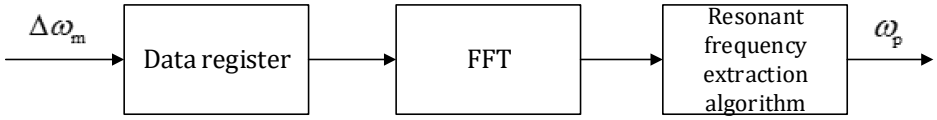

Figure 7. Structure diagram of resonance frequency detection part

3.1. Fast Fourier Transform (FFT)

Fast Fourier Transform (FFT) is an algorithm for computing the Discrete Fourier Transform (DFT) of a sequence or its inverse (IDFT). Fourier analysis converts a signal from its original domain (usually time or space) to the frequency domain. The DFT is computed by decomposing a set of values into components of different frequencies. This method is useful in many fields, but direct computation from the definition is generally too slow and impractical. The FFT computes this transform efficiently by factorizing the DFT matrix into a product of sparse (mostly zero) factors. It reduces the complexity of computing the DFT from $O\left(N^2\right)$ to $O\left(N\log N\right)$, where N is the data size. If the direct DFT were used instead, the computational complexity would increase significantly. Especially for long datasets, where N is in the order of thousands or millions, the difference in speed between the two algorithms is enormous. In the presence of round-off errors, many FFT algorithms are also much more accurate than direct or indirect computation of the DFT definition.

The radix-2 FFT is the simplest and most common form of the FFT algorithm. The radix-2 DIT computes the DFT of size N by dividing it into two interleaved DFTs of size $N/2$ at each recursive stage (hence the name "radix-2"). The algorithm is further divided into two methods: Decimation-in-Time (DIT-FFT) and Decimation-in-Frequency (DIF-FFT).

3.2. Radix-2 FFT Algorithm with Decimation-In-Time

Assume that the length of the time sequence $x\left(n\right)$ satisfies $N=2^m$, where m is a positive integer, and its DFT sequence is

$$X\left(k\right)=DFT\left[x\left(n\right)\right]=\sum_{n=0}^{N-1}x\left(n\right)W_N^{nk}\quad k=0,1,\cdots,N-1 \tag{7}$$

ISSN: 2472-3703 DOI: 10.6911/WSRJ.202604_12(4).0002

The sequence $x(n)$ is divided into two sequences according to the parity of the index n, and its DFT is given by

$$\begin{aligned} X(k) &= \sum_{r=0}^{(N/2)-1} x(2r) W_N^{2rk} + \sum_{r=0}^{(N/2)-1} x(2r+1) W_N^{(2r+1)k} \\ &= \sum_{r=0}^{(N/2)-1} x(2r) \left(W_N^2\right)^{rk} + W_N^r \sum_{r=0}^{(N/2)-1} x(2r+1) \left(W_N^2\right)^{rk} \end{aligned} \tag{8}$$

According to the reducibility of the twiddle factor, i.e., $W_N^2 = W_{N/2}$, the above equation can be simplified as

$$\begin{aligned} X(k) &= \sum_{r=0}^{(N/2)-1} x(2r) \left(W_{N/2}\right)^{rk} + W_N^r \sum_{r=0}^{(N/2)-1} x(2r+1) \left(W_{N/2}\right)^{rk} \\ &= X_1(k) + W_N^k X_2(k) \quad k = 0,1,\cdots,N-1 \end{aligned} \tag{9}$$

where $X_1(k)$ and $X_2(k)$ are the $N/2$-point DFTs of the even-indexed and odd-indexed sequences of sequence $x(n)$, respectively. It can be seen from the above equation that with this decomposition method, the results can be recombined into an N-point DFT. However, since the sequence length of $X(k)$ is N, and the sequence lengths of $X_1(k)$ and $X_2(k)$ are $N/2$, Equation (9) only yields the first $N/2$ results. Using the periodicity of the twiddle factor, i.e., $W_{N/2}^{rk} = W_{N/2}^{r(k+N/2)}$, we obtain

$$X_1\left(\frac{N}{2}+k\right) = X_1(k) \quad k = 0,1,\cdots,\frac{N}{2}-1 \tag{10}$$

$$X_2\left(\frac{N}{2}+k\right) = X_2(k) \quad k = 0,1,\cdots,\frac{N}{2}-1 \tag{11}$$

Equation (10) and Equation (11) show that the latter $N/2$ points of $X_1(k)$ and $X_2(k)$ are equal to the corresponding $X_1(k)$ and $X_2(k)$ of the former $N/2$ points, respectively. In addition, according to the symmetry of the twiddle factor

$$W_N^{k+N/2} = e^{-j\pi} W_N^k = -W_N^k \tag{12}$$

According to Equations (10), (11) and (12), we can obtain

$$\begin{aligned} X(k) &= X_1(k) + W_N^k X_2(k) \\ X(k+N/2) &= X_1(k) - W_N^k X_2(k) \end{aligned} \quad k = 0,1,\cdots,\frac{N}{2}-1 \tag{13}$$

ISSN: 2472-3703 DOI: 10.6911/WSRJ.202604_12(4).0002

The operation in the above equation is called a butterfly operation. The signal flow graph of the butterfly operation is shown in Figure 8.

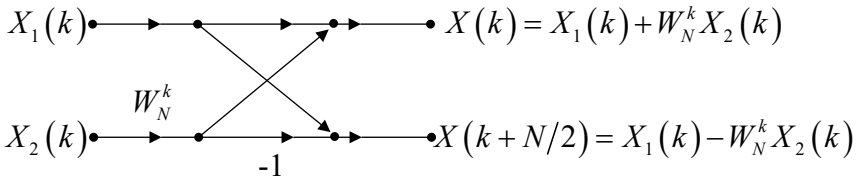

Figure 8. Butterfly operation signal flow chart

The DFT sequence of $N=8$ can be divided into two groups of $N=4$-point DFT sequences, $x_1(k)$ and $x_2(k)$, as shown in Figure 8. These two sequences can be further decomposed into four groups of $N=2$-point DFT sequences using the same decomposition method. Each $N=2$ sequence is processed according to the method shown in Figure 7, and finally a $N=8$-point DFT sequence can be obtained. The complete signal flow graph of the $N=8$-point FFT is shown in Figure 9.

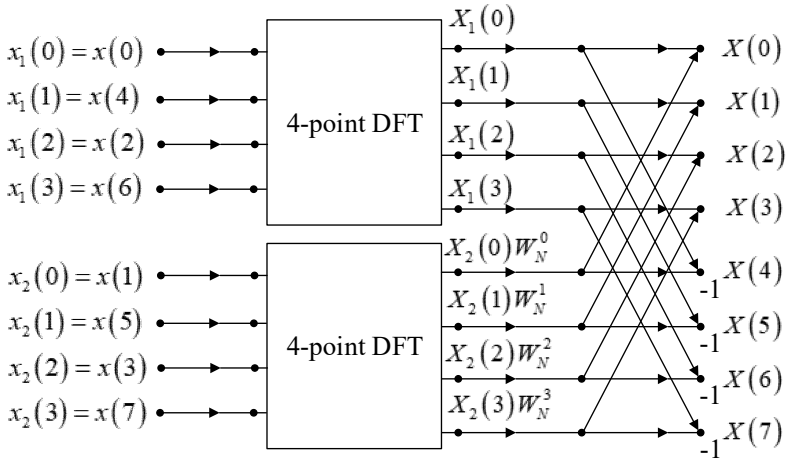

Figure 9. N=8 converted to 2 N=4 FFT signal flow chart

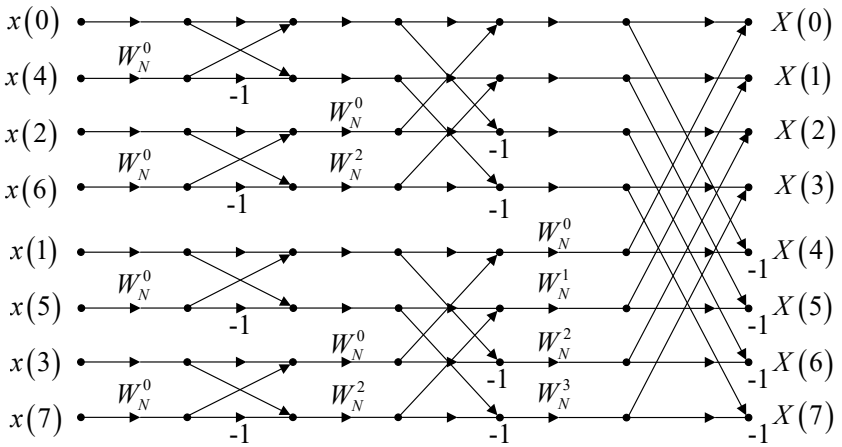

Figure 10. N=8 DFT-FFT signal flow diagram

ISSN: 2472-3703 DOI: 10.6911/WSRJ.202604_12(4).0002

3.3. Radix-2 FFT Algorithm with Decimation-In-Frequency

Assume that the length of the time sequence $x(n)$ satisfies $N=2^m$, where m is a positive integer. The sequence $x(n)$ is divided into two parts in the order of index n,

$$\begin{aligned} X(k) &= DFT\left[x(n)\right] = \sum_{n=0}^{(N/2)-1} x(n)W_N^{nk} + \sum_{n=N/2}^{N-1} x(n)W_N^{nk} \\ &= \sum_{n=0}^{(N/2)-1} \left[x(n) + W_N^{kN/2} x(n+N/2)\right] W_N^{nk} \end{aligned} \tag{14}$$

Since $W_N^{kN/2} = (-1)^k$, the above equation can be simplified as

$$X(k) = \sum_{n=0}^{(N/2)-1} \left[x(n) + (-1)^k x(n+N/2)\right] W_N^{nk} \tag{15}$$

According to different values of k, the sequence $X(k)$ can be divided into even-indexed and odd-indexed parts,

$$\begin{aligned} X(2r) &= \sum_{N=0}^{(N/2)-1} \left[x(n) + x(n+N/2)\right] W_N^{2rn} \\ X(2r+1) &= \sum_{N=0}^{(N/2)-1} \left[x(n) - x(n+N/2)\right] W_N^n W_N^{2rn} \end{aligned} \qquad r = 0,1,\cdots,\frac{N}{2}-1 \tag{16}$$

According to the reducibility of the twiddle factor, $W_N^{2m} = W_{N/2}^m$, the above equation can be written as

$$\begin{aligned} X(2r) &= \sum_{N=0}^{(N/2)-1} \left[x(n) + x(n+N/2)\right] W_N^{rn} \\ X(2r+1) &= \sum_{N=0}^{(N/2)-1} \left[x(n) - x(n+N/2)\right] W_N^n W_N^{rn} \end{aligned} \qquad r = 0,1,\cdots,\frac{N}{2}-1 \tag{17}$$

Let

$$\begin{aligned} x_1(n) &= x(n) + x(n+N/2) \\ x_2(n) &= x(n) - x(n+N/2) W_N^n \end{aligned} \qquad r = 0,1,\cdots,\frac{N}{2}-1 \tag{18}$$

Substituting Equation (17) into Equation (18), we can obtain

ISSN: 2472-3703 DOI: 10.6911/WSRJ.202604_12(4).0002

$$\begin{aligned} X(2r) &= \sum_{N=0}^{(N/2)-1} x_1(n) W_N^{rn} \\ X(2r+1) &= \sum_{N=0}^{(N/2)-1} x_2(n) W_N^{rn} \end{aligned} \qquad r = 0,1,\cdots,\frac{N}{2}-1 \tag{19}$$

As shown in Figure 11, the operation in the above equation can be represented by the signal flow of a butterfly operation

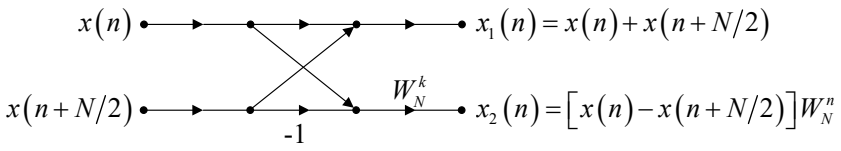

Figure 11. Base-2 DIF-FFT signal flow diagram

The DFT sequence $x(n), n = 0,1,\cdots,8$ of $N = 8$ is divided into two front and rear sequences in natural order. These two sequences are further divided in the same way into four groups with two sequences per group. Its signal flow is shown in Figure 12.

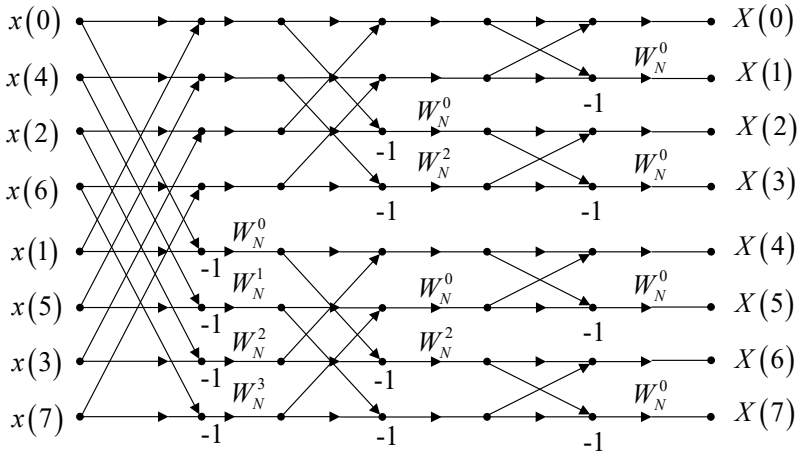

Figure 12. N=8 sequence base-2 DIF-FFT signal flow diagram

4. NOTCH FILTER DESIGN

The transfer function of a traditional notch filter is

$$G(s) = \frac{s^2 + (2\pi f)^2}{s^2 + 2\pi k s + (2\pi f)^2} \tag{20}$$

where f is the notch center frequency and k is the notch width.

When the notch center frequency $f = 10\text{Hz}$ and notch width k are 1, 4, and 8 respectively, the Bode plot of the system is shown in Figure 13.

ISSN: 2472-3703 DOI: 10.6911/WSRJ.202604_12(4).0002

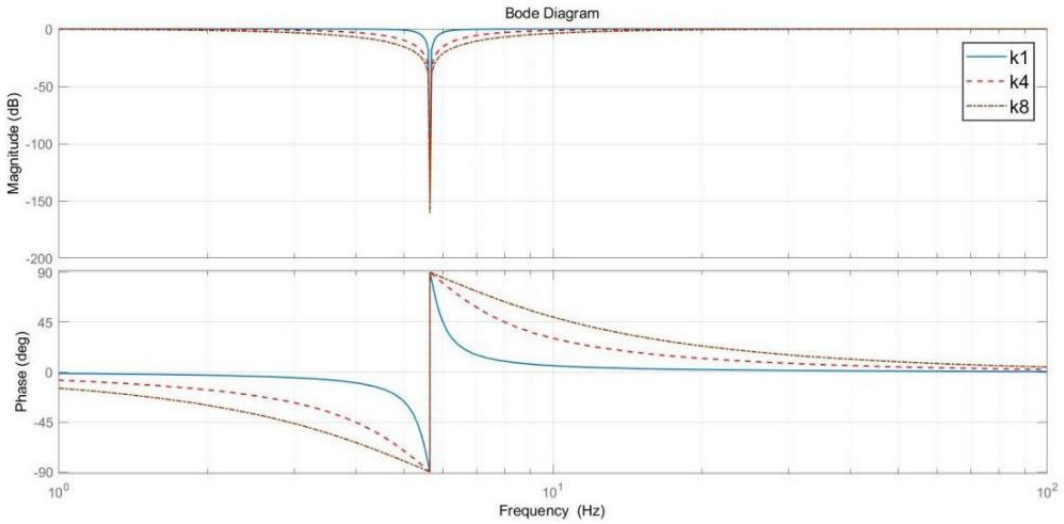

Figure 13. Bode diagram of notch filter with different notch width

It can be seen from Figure 13 that the notch filter can greatly reduce the amplitude of the system at the notch center without affecting other frequencies. However, it causes abrupt changes in amplitude and phase at the notch center, which can significantly degrade the system performance. Moreover, both the notch center and width of the traditional notch filter are adjusted by parameter k, which is very unintuitive and inconvenient. Therefore, it is necessary to improve the notch filter.

The transfer function of the improved filter is

$$G(s)=\frac{s^2+2\pi\zeta ks+(2\pi f)^2}{s^2+2\pi ks+(2\pi f)^2} \tag{21}$$

where f is the notch center frequency, ξ is the depth parameter, and k is the width parameter. The improved filter can achieve a magnitude attenuation of $20\lg|\xi|$ dB at the notch center frequency, while the width at which the magnitude drops by 3 dB is k.

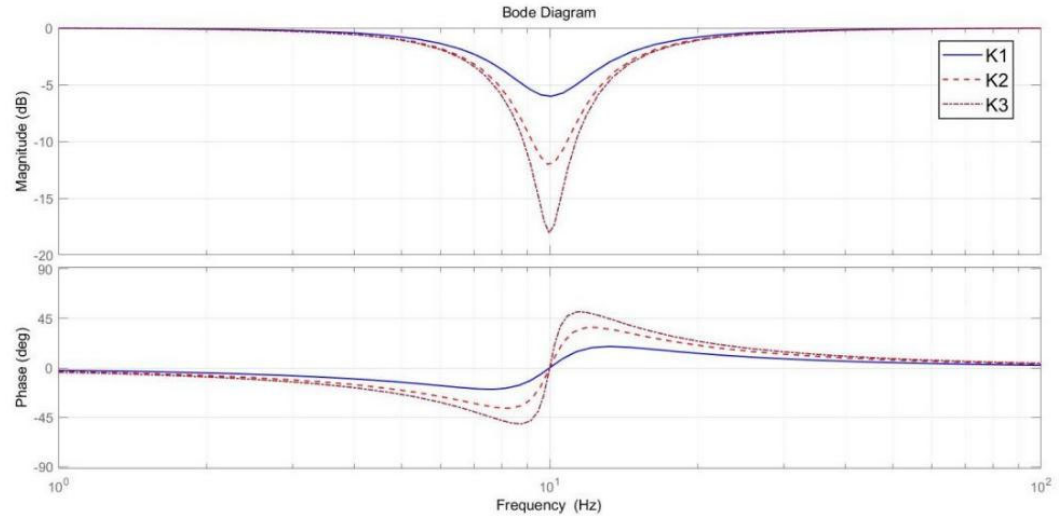

Figure 14. Bode diagram of notch filter with different depth parameters

ISSN: 2472-3703 DOI: 10.6911/WSRJ.202604_12(4).0002

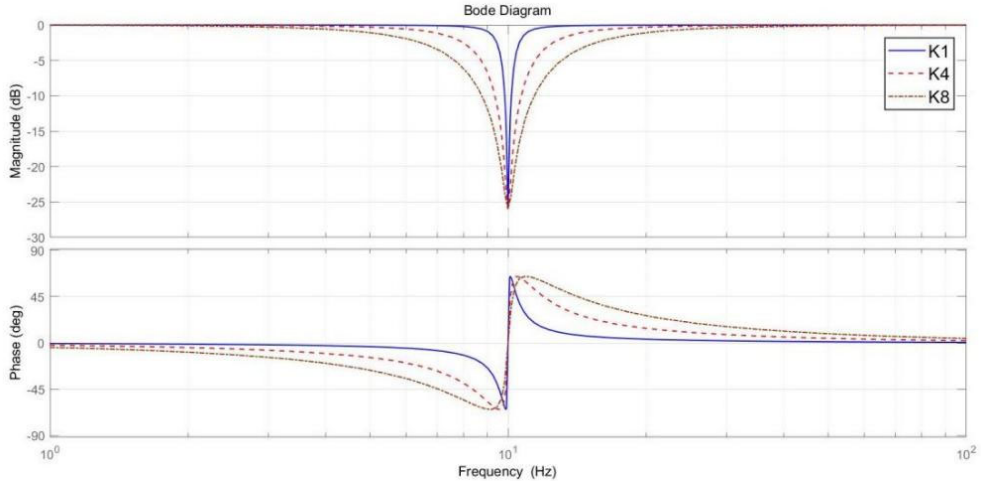

Figure 15. Bode diagram of notch filter with different notch width

Figure 14 shows the Bode plots of the system with different values of ξ under fixed $f=10\text{Hz}$ and $k=8$. Here, K1 represents $\xi=0.5$, K2 represents $\xi=0.25$, and K3 represents $\xi=0.05$. It can be seen from the figure that, with the center frequency and width parameter unchanged, the amplitude attenuation of the system increases gradually as the depth parameter ξ decreases. Figure 15 shows the Bode plots of the system with different values of k under fixed $f=10\text{Hz}$ and $\xi=0.05$. Here, K1 represents $k=1$, K4 represents $k=4$, and K8 represents $k=8$. It can be seen that, with the center frequency and depth parameter unchanged, the width between the 3-dB amplitude drop points becomes wider as the width parameter increases. It can be observed from Figures 14 and 15 that the notch width and depth of the improved notch filter can be adjusted independently, which greatly improves the situation of the traditional notch filter where only one parameter can be modified.

4.1. Effect of Notch Filter on System Performance

Substituting $s=j\omega$ into the transfer function in Equation (20), the amplitude-frequency characteristic can be obtained as

$$G(j\omega)=\frac{(j\omega)^2+j2\pi\zeta k\omega+(2\pi f_0)^2}{(j\omega)^2+j2\pi k\omega+(2\pi f_0)^2} \tag{22}$$

its amplitude is

$$\left|G(jf)\right|=\sqrt{\frac{\left(f_0^2-f^2\right)^2-(\zeta kf)^2}{\left(f_0^2-f^2\right)^2-(kf)^2}} \tag{23}$$

Its phase-frequency characteristic is

$$\varphi(jf)=\begin{cases}\arctan\dfrac{\xi kf}{f_0^2-f^2}-\arctan\dfrac{kf}{f_0^2-f^2}, f\neq f_0\\ 0, f=f_0\end{cases} \tag{24}$$

ISSN: 2472-3703 DOI: 10.6911/WSRJ.202604_12(4).0002

When the notch center frequency f of the notch filter in the system is greater than the cutoff frequency ω_c of the system itself, the phase angle loss caused by the filter at the system cutoff frequency is

$$\varphi(jf) = \arctan\frac{\xi k\omega_c}{f_0^2 - \omega_c^2} - \arctan\frac{k\omega_c}{f_0^2 - \omega_c^2} \tag{25}$$

Let

$$\tan\alpha = \frac{\xi k\omega_c}{f_0^2 - \omega_c^2}, \tan\beta = \frac{k\omega_c}{f_0^2 - \omega_c^2} \tag{26}$$

It can be obtained that

$$\tan(\alpha - \beta) = \frac{\tan\alpha - \tan\beta}{1 + \tan\alpha\tan\beta} = \frac{(\xi - 1)k\omega_c\left(f_0^2 - \omega_c^2\right)}{\zeta k\omega_c^2 + \left(f_0^2 - \omega_c^2\right)^2} \tag{27}$$

Its inverse function is

$$\begin{aligned}(\alpha - \beta) &= \arctan\frac{\xi k\omega_c}{f_0^2 - \omega_c^2} - \arctan\frac{k\omega_c}{f_0^2 - \omega_c^2} \\ &= \arctan\frac{(\xi - 1)k\omega_c\left(f_0^2 - \omega_c^2\right)}{\xi k\omega_c^2 + \left(f_0^2 - \omega_c^2\right)^2}\end{aligned} \tag{28}$$

The phase angle loss at the system cutoff frequency is

$$\varphi = \arctan\frac{(\xi - 1)k\omega_c\left(f_0^2 - \omega_c^2\right)}{\xi k\omega_c^2 + \left(f_0^2 - \omega_c^2\right)^2} \tag{29}$$

When the value of k is small, the above equation can be simplified as

$$\varphi = -\arctan\frac{k\omega_c}{f_0^2 - \omega_c^2} \tag{30}$$

It can be seen from Equation (29) that the phase angle loss caused by the filter at the system cutoff frequency is inversely proportional to the depth parameter and proportional to the width parameter. Therefore, to minimize the influence of the filter on the system, a larger depth parameter and a smaller width parameter should be selected, so that the phase of the system at the cutoff frequency will not change significantly.

4.2. Method for Determining Parameters of Notch Filter

According to the previous content in this chapter, when resonance occurs in a dual-inertia mechanical system, the resonance frequency can be obtained through FFT analysis. Then, a

ISSN: 2472-3703 DOI: 10.6911/WSRJ.202604_12(4).0002

notch filter is used to attenuate the amplitude at this resonance frequency, so as to achieve the effect of resonance suppression. Furthermore, the filtering performance can be adjusted by tuning the notch center frequency f, notch width k, and notch depth ζ of the filter, so as to realize mechanical resonance suppression without affecting other performances of the system.

(1) Method for determining the center frequency f

Since the center frequency f is the frequency at which the notch filter takes effect, the center frequency f should be set at the resonant frequency of the system. The determination of this parameter is relatively simple and convenient. Let the resonant frequency of the system obtained by FFT analysis be f_0, then

$$f = f_0 \tag{31}$$

(2) Method for determining the notch width k

Since the resonant frequency of the system mostly appears in the form of a frequency band, that is, the amplitudes at frequencies near the resonant point are also relatively high, it is necessary to appropriately broaden the filtering range of the filter. This can smooth the amplitude-frequency characteristic curve of the system and avoid the problem of resonant frequency offset caused by insufficient notch width. However, the notch width cannot be increased indefinitely. As can be seen from Equation (29), the phase angle loss caused by the filter at the system cutoff frequency is proportional to the width parameter. In other words, the larger the notch width, the greater the phase angle loss. Excessively large notch width will degrade the robustness of the system and even lead to system instability. Therefore, the selection of the notch width requires an appropriate range.

Let the threshold of system resonance be H_1, that is, mechanical resonance occurs where the amplitude is greater than H_1. Let the system frequencies at which the amplitude reaches H_1 on the left and right sides around f_0 be f_1 and f_2 respectively. Then the method for determining the notch width k is

$$k = 2\max\left\{\left(f_0 - f_1\right),\left(f_2 - f_0\right)\right\} \tag{32}$$

(3) Method for determining the notch depth ζ

The notch filter can reduce the amplitude at the notch center frequency by a maximum value of $20\lg|\zeta|$. It can be seen that within the range from 0 to 1, the notch depth ζ should be as small as possible. However, an excessively small notch depth will also increase the phase angle loss at the system cutoff frequency, so an appropriate range must be determined. The filter can be considered to have taken effect when the amplitude is less than H_1. Let the amplitude at the system frequency f_0 be $H_{\max}$, since

$$H_1 = H_{\max} \cdot \zeta \tag{33}$$

Therefore

ISSN: 2472-3703 DOI: 10.6911/WSRJ.202604_12(4).0002

$$\zeta = \frac{H_1}{H_{\max}} \tag{34}$$

4.3. Digital Implementation of Notch Filter

In practical applications, the control of mechanical resonant systems mainly adopts the digital control method. The notch filter must be discretized before digital implementation. Let $s = \frac{2}{T}\frac{z-1}{z+1}$ in Equation (21) be given, then

$$\frac{y(k)}{u(k)} = \frac{d_2 + d_1 z^{-1} + d_0 z^{-2}}{1 + c_1 z^{-1} + c_0 z^{-2}} \tag{35}$$

Rewrite it in the form of a difference equation,

$$y(k) = -c_0 y(k-2) - c_1 y(k-1) + d_0 u(k-2) + d_1 u(k-1) + d_2 u(k) \tag{36}$$

Its corresponding discrete coefficients are

$$\begin{cases} c_0 = \dfrac{4/T^2 - 4\pi k/T + (2\pi f)^2}{4/T^2 + 4\pi k/T + (2\pi f)^2} \\ c_1 = \dfrac{2(2\pi f)^2 - 8/T^2}{4/T^2 + 4\pi k/T + (2\pi f)^2} \\ d_0 = \dfrac{4/T^2 - 4\pi k\zeta/T + (2\pi f)^2}{4/T^2 + 4\pi k/T + (2\pi f)^2} \\ d_1 = \dfrac{-8/T^2 + 2(2\pi f)^2}{4/T^2 + 4\pi k/T + (2\pi f)^2} \\ d_2 = \dfrac{4/T^2 + 4\pi k\zeta/T + (2\pi f)^2}{4/T^2 + 4\pi k/T + (2\pi f)^2} \end{cases} \tag{37}$$

where T is the sampling period.

5. EXPERIMENT VERIFICATION

(1) To verify the effectiveness of the vibration suppression control algorithm, an experimental platform with a high-inertia load for robotic arms was constructed. The platform consists of a servo motor-harmonic drive joint (the second joint of an industrial robot) composed of a 750 W servo motor and a 101:1 harmonic reducer, a high-inertia robotic arm load, a servo drive, a Beckhoff EtherCAT controller, and a TwinCAT host computer. The servo motor and harmonic reducer are connected via a belt pulley, which introduces a certain degree of flexibility into the system. The entire robotic arm is moved to a vertical position and locked by the controller to maximize the load inertia of the second joint. The servo drive is set to position mode, and the corresponding motion command program is edited on the TwinCAT host computer and sent to the EtherCAT controller. The EtherCAT controller controls the drive via the EtherCAT protocol to actuate the motor-belt pulley-harmonic drive joint (second joint) to

ISSN: 2472-3703 DOI: 10.6911/WSRJ.202604_12(4).0002

swing back and forth within 90°. During this process, the load exerted on the motor-belt pulley-harmonic drive joint varies with the angular position of the robotic arm, thus forming a high-inertia flexible time-varying load experimental platform.

(2) Different rotational speeds are assigned to the second joint via the TwinCAT host computer (from 50 r/min to 3000 r/min, with an interval of 50 r/min for each given speed). Experiments at various speed ranges show that obvious vibration occurs in the robotic arm within 2.5 seconds when the second joint moves downward from the vertical position at a given motor speed of 350 r/min. The actual motor speed waveform under this working condition is plotted via the TwinCAT host computer, as shown in Figure 16. Figure 16a shows the actual speed waveform during the entire up and down swing process, and Figure 16b shows the locally magnified experimental waveform during the vibration phase when moving downward from the vertical position. It can be seen from the locally magnified waveform in Figure 16b that the actual motor speed fluctuates significantly during this interval, which corresponds to the resonance region of the entire motor-pulley-harmonic drive joint. The waveform during the vibration interval is processed by FFT analysis, and the resulting FFT curve is shown in Figure 18a. It can be seen from Figure 18a that a resonant frequency peak at approximately 10 Hz exists within this motion interval. On this basis, the vibration suppression control algorithm is integrated into the servo drive. The magnified actual speed waveform under the same working condition with the vibration suppression algorithm is shown in Figure 17. By comparing Figure 17 with Figure 16a, the actual speed fluctuation is almost completely eliminated after applying the vibration suppression control algorithm, and the speed waveform becomes relatively smooth. The waveform after vibration suppression is also analyzed by FFT, as shown in Figure 18b. By comparing Figure 18a and Figure 18b, the resonant frequency peak disappears after adding the algorithm, and the servo system with the vibration suppression control algorithm has no obvious influence on the waveforms at other speed ranges. The experimental results verify the effectiveness and practicability of the proposed vibration suppression control algorithm.

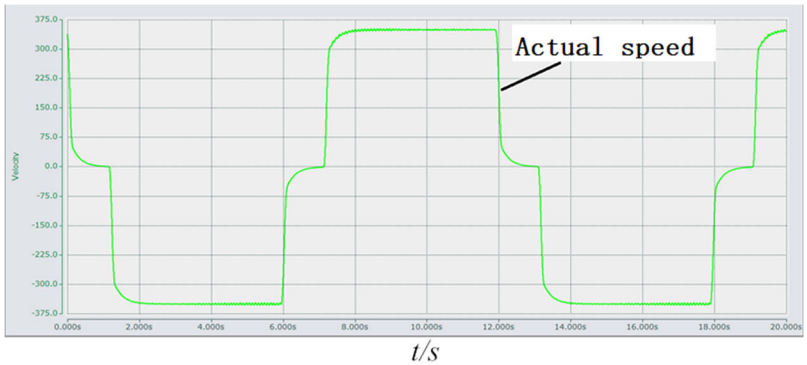

(a) overall waveform

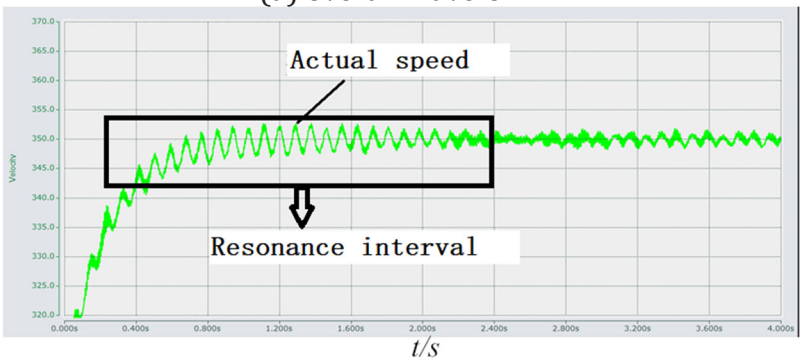

(b) Local amplified resonance waveform

Figure 16. Actual speed waveform under large inertia load (350r/min)

ISSN: 2472-3703 DOI: 10.6911/WSRJ.202604_12(4).0002

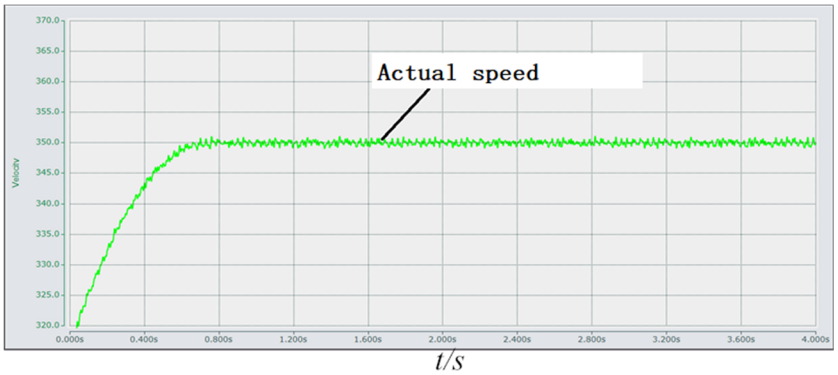

Figure 17. Actual speed amplification waveform after adding the vibration suppression control algorithm (350r/min)

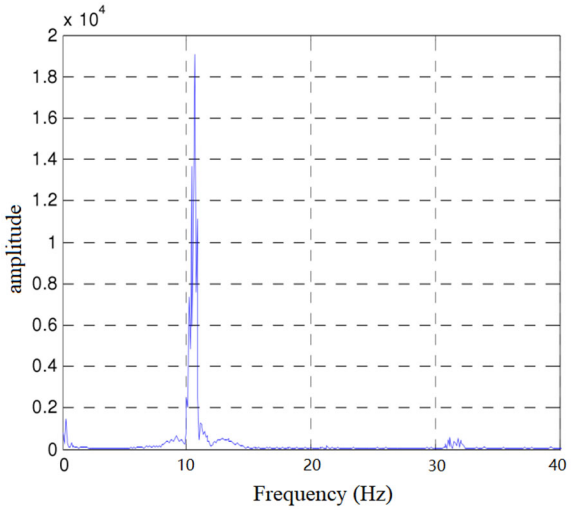

(a) FFT analysis curve before adding the vibration suppression algorithm

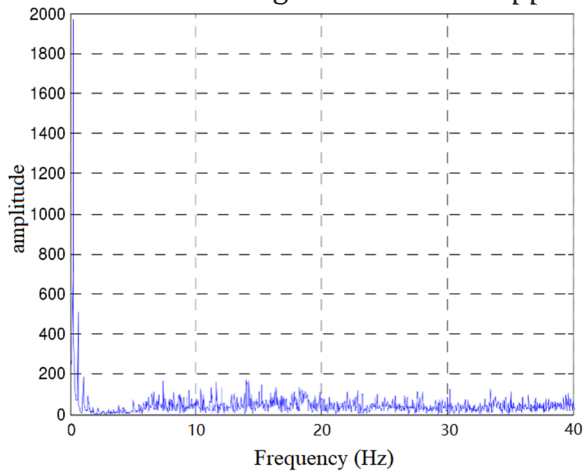

(b) FFT analysis curve after adding the vibration suppression algorithm

Figure 18. FFT analysis curve of speed waveform

6. CONCLUSION

This paper analyzes the mechanical resonance in permanent magnet AC servo systems and identifies the main factors affecting resonance. Furthermore, the fast Fourier transform is adopted for online frequency identification of the resonant system. Finally, a notch filter is used to filter out the resonant frequency of the system. The influence of the notch filter on the system

ISSN: 2472-3703 DOI: 10.6911/WSRJ.202604_12(4).0002

is analyzed, the parameters of the filter are determined, and the digital implementation of the notch filter is completed. Through the analysis of the mechanical resonant system and online identification of the resonant frequency, the inherent mechanical resonance of the permanent magnet AC servo system is effectively suppressed, and the performance of the system is improved.

ACKNOWLEDGMENTS

The authors thank the editor and anonymous reviewers for their valuable remarks and helpful suggestions. This study was partially supported by the Provincial Research Platform Opening Fund of Yancheng Polytechnic College (YGKF202201).

REFERENCES

[1] S. Katsura and K. Ohnishi: Force Servoing by Flexible Manipulator Based on Resonance Ratio Control, IEEE Transactions on Industrial Electronics, Vol. 54 (2007) No.1, p.539-547.

[2] R. Muszynski and J. Deskur: Damping of Torsional Vibrations in High-Dynamic Industrial Drives, IEEE Transactions on Industrial Electronics, Vol. 57 (2009) No.2, p.544-552.

[3] T. Orlowska-Kowalska and M. Kaminski: Effectiveness of Saliency-Based Methods in Optimization of Neural State Estimators of the Drive System with Elastic Couplings, IEEE Transactions on Industrial Electronics, Vol. 56 (2009) No.10, p.4043-4051.

[4] K. Jezernik and A. Sabanovic: SMC with Disturbance Observer for a Linear Belt Drive, IEEE Transactions on Industrial Electronics, Vol. 54 (2007) No.6, p.3402-3412.

[5] M. Cychowski, K. Szabat and T. Orlowska-Kowalska: Constrained Model Predictive Control of the Drive System with Mechanical Elasticity, IEEE Transactions on Industrial Electronics, Vol. 56 (2009) No.6, p.1963-1973.

[6] H.J. Shin, J.Y. Choi, H.W. Cho, et al.: Effects of Mechanical Resonance on Vibrations of Mechanical Systems with Permanent Magnet Machines, IEEE Transactions on Magnetics, Vol. 50 (2014) No.11, p.1-4.

[7] J. Zheng, Y. Feng and X. Yu: Mechanical Resonance Suppressing Method for PMSM System Based on High-Order Sliding Modes, *IECON 2007-33rd Annual Conference of the IEEE Industrial Electronics Society* (Taiwan, 2007), p.704-709.

[8] R. Li and X. Ren: Mechanical Resonance Modeling and Forecasting in Servo Systems Based on Vector Fitting, *2013 International Conference on Mechanical and Automation Engineering* (Jiujang, China, 2013), p.66-69.

[9] Y. Chen, M. Yang, K. Hu, et al.: Suppression of Mechanical Resonance in Digital Servo System Considering Oscillation Frequency Deviation, *IECON 2017-43rd Annual Conference of the IEEE Industrial Electronics Society* (Florence, Italy, 2017), p.2201-2206.

[10] Y. Chen, M. Yang, Y. Sun, et al.: A Modified Full-Band Adjustable Bi-Quad Filter for Mechanical Resonance Suppression in Industrial Servo Drive Systems, *2019 IEEE Industry Applications Society Annual Meeting* (2019), p.1-6.

[11] M. Wang, X. Liu, X. Dong, et al.: A Novel Method to Detect and Suppress Mechanical Resonance for Servo System, *2016 9th International Symposium on Computational Intelligence and Design (ISCID)* (Hangzhou, China, 2016), Vol. 1, p.349-354.